W.G. Yang et al., Intermetallics, 151 (2022) 107691
https://doi.org/10.1016/j.intermet.2022.107691

V_8SiB_4 – A new ternary phase in the V–Si–B system

W.G. Yang[1], R.S. Touzani[2,*], G. Hasemann[2], M. Yazlak[3], M. Ziegner[1], B. Gorr[4], R. Schwaiger[1,5], M. Krüger[2]

[1] *Forschungszentrum Jülich GmbH, Institute of Energy and Climate Research, Microstructure and Properties of Materials (IEK−2), Leo-Brand-Str.1, 52425, Jülich, Germany*

[2] *Otto-von-Guericke University Magdeburg, Institute of Materials and Joining Technology, Universitätsplatz 2, 39106, Magdeburg, Germany*

[3] *University Siegen, Institute of Materials Technology, Paul-Bonatz-Strasse 9-11, 57076, Siegen, Germany*

[4] *Karlsruhe Institute of Technology, Institute for Applied Materials – Applied Materials Physics (IAM−AWP), Hermann-von-Helmholtz-Platz 1, 76344, Eggenstein-Leopoldshafen, Germany*

[5] *Chair of Energy Engineering Materials, Faculty 5, RWTH Aachen University, Templergraben 55, 52056, Aachen, Germany*

Highlights

- A new ternary phase, V_8SiB_4, was found in the V_{ss}–V_3Si–V_5SiB_2 phase region at 1600 °C after heat treatment at 1400 °C for 100 h and 200 h.
- By combining EDS, XRD and DFT calculations, we determined the crystal structure of V_8SiB_4, which may represent a new crystallographic prototype.
- The stability of V_8SiB_4 at 0 K was examined using DFT.

Abstract

The present study reports on the existence of a new ternary phase, V_8SiB_4, in the V−Si−B system. The new phase was found in alloys heat-treated at 1400 °C for 100 h and 200 h within the V_{ss}–V_3Si–V_5SiB_2 phase field at 1600 °C. The crystal structure of V_8SiB_4 was determined by combining energy-dispersive X-ray spectroscopy (EDS), X-ray diffraction (XRD) and density functional theory (DFT) calculations. To further examine the stability of V_8SiB_4, electronic density-of-states (EDOS), phononic density-of-states (PDOS), the chemical bonding and the elastic properties of V_8SiB_4 were calculated using DFT and compared with the properties of V_5SiB_2 (T2).

Keywords

Intermetallics; crystal chemistry; heat treatment; X-ray diffraction; density functional theory; phase stability

*E-mail address: rachid.touzani@ovgu.de

1 Introduction

Refractory metals (RM), such as Cr, Nb, Ta, Mo or V, and their compounds, are currently in the spotlight as promising candidates in the design of new high temperature alloys. For example, the RM−Si−B systems exhibit great potential due to the high melting point of the refractory metal and the additional creep- and oxidation resistance provided by intermetallic compounds, especially RM−silicides and RM−Si−borides [1–6]. In certain equilibria within the Nb/Ta/Mo/V−Si−B systems, among the RM−Si−borides the $RM_5Si_{3-x}B_x$ (T2) phases might be highly beneficial, because the T2 phases can coexist with the RM solid solution (RM_{ss}) phases [7–12] which leads to a compromise between the ductility provided by the RM_{ss} phases and the brittleness caused by the T2 phases.

The crystallographic prototype of the T2 phase is the crystal structure of Cr_5B_3, where Cr atoms are located on the Wyckoff sites 4c and 16l of the space group *I*4/*mcm* (No.140) and B atoms on Wyckoff sites 4a and 8h [13]. In the Cr_5B_3, however, Si atoms can replace the B atoms only at the 4a sites of the crystal structure of Cr_5B_3 [14]. Therefore, the phase region of $Cr_5Si_xB_{3-x}$ (x =0-1) is expanded along Cr_5B_3−Cr_5SiB_2, which was observed experimentally after heat treatment at 1300 °C [10]. By contrast, in the isothermal section of the Cr−Si−B system at 1300 °C [10], the Cr_5Si_3 phase is not a T2 phase but a so-called T1 phase due to its W_5Si_3-type ($D8_m$) structure, also belonging to the space group *I*4/*mcm* (No.140) [15].

Parthé et al. [16] investigated T2 phases (Nb_5Si_3 and Ta_5Si_3), in which the B atoms were fully substituted by Si in the $D8_l$ structure. By adding B to Nb_5Si_3 to replace the Si atoms located on the 8h sites [17], the ternary intermetallic phase $Nb_5Si_{3-x}B_x$ (x = 0-2) is formed and its composition changes approximately along Nb_5Si_3−Nb_5SiB_2 in the isothermal section of the Nb−Si−B system at 1600 °C [7]. The phase region of $Nb_5Si_{3-x}B_x$ becomes an almost linear region by connecting the stoichiometric composition of Nb_5Si_3 and Nb_5SiB_2 at 1700 °C [8]. Similarly, the phase region of $Ta_5Si_{3-x}B_x$ can be expanded along Ta_5Si_3−Ta_5SiB_2 as it was observed in the isothermal section of the Ta−Si−B system at 2000 °C [9].

Unlike the Cr/Nb/Ta−Si−B systems, $(Mo/V)_5B_3$ phases have not been discovered, while the corresponding $(Mo/V)_5Si_3$ (T1) phases with $D8_m$ structure and $(Mo/V)_5SiB_2$ (T2) phases with $D8_l$ structure were reported in the Mo/V−Si−B systems [11,12,18]. In the isothermal section of the Mo−Si−B system at 1600 °C [11] or 1800 °C [12], the phase region of the $Mo_5Si_{3-x}B_x$ is restricted to a small region close to

the stoichiometric composition of Mo_5SiB_2. By contrast, the B-content of $V_5Si_{3-x}B_x$ could be varied from 25 at% to 32 at% assuming a V_5B_3–V_5SiB_2 (T2) concentration line in the isothermal section of V−Si−B system at 1600 °C [18]. A possible reason for the expansion of the $V_5Si_{3-x}B_x$ phase region along the assumed V_5B_3–V_5SiB_2 (T2) but not along V_5Si_3–V_5SiB_2 (T2) is that the assumed V_5B_3 with a $D8_l$ structure could be slightly more stable than that with a $D8_8$ or $D8_m$ structure according to density functional theory calculations [19]. Compared with the V_3B_2 phase with $D5_a$ structure on the V−B side, however, the existence of a V_5B_3 phase is rather unlikely [19].

The aim of this work is to investigate the crystal structure and chemical composition of a new ternary phase in the V−Si−B system and elucidate its similarity with the phase V_5SiB_2 (T2), which is in equilibrium with V_{ss} and V_3Si at 1600 °C [18]. Different experimental techniques including electron backscatter diffraction, energy-dispersive X-ray spectroscopy and X-ray diffraction were applied. Electronic density-of-states and phononic density-of-states of the new ternary phase, its chemical bonding and the elastic properties were studied by density functional theory calculations and are compared with V_5SiB_2.

2 *Experiments and Methods*

2.1 Synthesis and phase identification

In this work, three different variants of V−5Si−9B alloy were fabricated, namely as-cast and heat-treated at 1400 °C for 100 h and 200 h. Arc-melting was performed under flowing argon atmosphere after obtaining a vacuum of 10^{-2} mbar in the arc-melter. The flux of flowing argon gas was adjusted to maintain the argon gas pressure constant at 600 mbar at room temperature. The raw materials were carefully weighted using high-purity elemental turnings of V (99.7 wt.%) and granules of Si (99.99 wt.%) and B (99.0 wt.%) to produce a 15 g sample. The alloy was re-melted and flipped five times to ensure a homogeneous compositional distribution of all elements. A weight loss of < 1 wt.% indicated that the composition after arc-melting was very close to the nominal composition. After cutting the as-cast alloy into two pieces, one half was used to investigate the as-cast microstructure, while the other one was heat-treated at 1400 °C under high vacuum ($1.5 \cdot 10^{-5}$ mbar) for 100 h and 200 h; followed by furnace-cooling within 3 h below 200 °C to investigate the microstructure after the heat treatment. For metallographic preparation, the samples were embedded in a cold mounting resin (Expoy 2000, Cloeren Technology, Wegberg, Germany), subsequently ground down

to 2000 grit using SiC paper. The polishing was conducted with 15 μm, 6 μm, 3 μm and 1 μm diamond suspension, and finished using colloidal silica.

A Zeiss Merlin scanning electron microscope (SEM, Zeiss Microscopy, Oberkochen, Germany) was used to observe the microstructures using the secondary electron (SE) and the backscattered electron (BSE) mode. Electron backscatter diffraction (EBSD, Oxford Instruments, UK) was performed using the crystal structures of V_{ss}, V_3Si, V_5Si_3, V_3B_2, VB and V_5SiB_2 to determine the phases and obtain the phase mapping. Energy-dispersive X-ray spectroscopy (EDS, X-Max 150, Oxford Instruments, UK) was performed to quantitatively determine the chemical compositions of phases. The quantitative detection of B using EDS is challenging because of the low electron density of the B atom (5 electrons per atom [20]). It can be achieved, though, since no peak overlap of the B EDS spectra with the V or Si EDS spectra exists, in contrast to the Mo M_ζ-line (0.193 keV) which is close to the B K_α-line (0.183 keV) [21]. Furthermore, the B-content in $V_5Si_{3-x}B_x$ (T2) phases is high [18]. X-ray diffraction (XRD) measurements were performed on the polished bulk samples at room temperature using a D8 ADVANCE (Bruker, USA) and an EMPYREAN (Malvern Panalytical, UK) diffractometer to identify the crystal structures of phases. The lattice parameters of the phases were determined using the software GSAS-II [22] and the Pawley refinement [23], in which the intensities of the calculated diffraction peaks do not depend on the atomic positions in the crystal structure. Here, the main lattice planes of each crystal structure, which have easily distinguishable diffraction reflections according to the XRD-simulated patterns of each crystal structure, were used for the Pawley refinement. The XRD-simulations using the software GSAS-II [22] take into account both the unit cell and atomic positions of the crystal structure. The corresponding crystal structure data for the XRD-simulation were taken from the Inorganic Crystal Structure Database (ICSD) [24] with the collection codes 241937 [25], 87328 [26], 88317 [27] and 44490 [28] for V_{ss}, V_3Si, V_3B_2 and V_5SiB_2 phases, respectively.

2.2 *First principles calculations*

First-principles calculations were carried out with Quantum ESPRESSO (QE) [29,30] for the structural relaxation using the projector augmented waves (PAW) pseudopotentials [31] from the PSLibrary version 1.0.0 [32]. The kinetic energy cut-off of the plane waves was set to 100 Ry, while the cut-off for the charge density and potential was set to 400 Ry. The structural relaxation stopped until a total energy convergence of 10^{-6} Ry and a force convergence of 10^{-5} Ry/Bohr were reached. The Marzari-Vanderbilt cold smearing [33] and a Gaussian spreading of 0.01 Ry were

chosen to account for the Brillouin-zone integration. The k-mesh was divided by 10x10x4 for V_8SiB_4 using the Monkhorst-Pack algorithm [34]. Exchange and correlation in this density functional theory (DFT) -based method were treated with the generalized gradient approximation (GGA) functional as parameterized by Perdew, Burke and Ernzerhof (PBE-GGA) [35].

The elastic properties were determined with thermo_pw [36], a Fortran program using Quantum ESPRESSO routines as the underlying engine. To obtain the Voigt-Reuss-Hill [37–39] approximated bulk, shear and Young's moduli, the standard algorithm and frozen ions were used. To calculate the Vickers hardness, the formula by Tian et al. [40] was used.

To check the dynamical and mechanical stability, Quickstep [41] was used as implemented in the CP2K version 5.1 program package [42] as the calculator for PHONOPY [43]. The first-principles calculations for the structural relaxation using the Gaussian plane wave method (GPW) [44] were executed until a total energy self-consistency of 10^{-6} Ha and until the self-consistency for the forces and maximum geometry change of 10^{-5} Ha/Bohr and 10^{-5} Bohr, respectively were achieved. The energy cut-off for the plane waves on the grid was 1200 Ry and the k-mesh sampled via the aforementioned Monkhorst-Pack algorithm were 10x10x4 and 12x12x6 for the new phase and the V_5SiB_2 phase, respectively. For V, Si and B the DZVP-MOLOPT-SR-GTH basis set [45] was chosen for the atomic centered Gaussian functions, while for the interatomic part the GTH-pseudopotentials were used [46–48]. Exchange and correlation in this DFT-based method were treated with the PBE-GGA. For the PHONOPY calculations, we used structural relaxed 2x2x1 supercells and changed the k-mesh to 4x4x4 in the energy and force determination.

The calculations of the density-of-states and the chemical bonding analysis were then carried out using the tight-binding, linear muffin-tin orbitals with the atomic spheres approximation (TB-LMTO-ASA) [49,50] as implemented in the TB-LMTO 4.7 program [51]. Exchange and correlation were treated with the PW91-GGA functional by Perdew et al. [52]. The k-mesh was chosen to be 16x16x16 for the new phase and V_5SiB_2. The bonding analysis was done by calculation of the crystal orbital Hamilton population (COHP) and their integrals (ICOHP) [53]. Because –COHP values are plotted, negative –COHPs are antibonding states, positive ones are bonding states and non-bonding states have –COHPs of zero. The Fermi level (E_F) was set to 0 eV.

3 Results and discussion

3.1 Microstructural evolution, X-ray diffraction and phase composition analysis

The microstructures of the as-cast and heat-treated (1400 °C, 100/200 h) alloys V−5Si−9B are shown in Fig. 1 (a) - (c), respectively, whereby the phases were identified by EBSD and subsequently confirmed by EDS analyses. In the as-cast state, the binary V_{ss}−V_3B_2 and V_{ss}−V_5SiB_2 eutectic microstructures can be observed (Fig. 1 (a)), which were not found after the heat treatment at 1400 °C due to the decomposition of the V_3B_2 phase and the coarsening of the intermetallic phases (Fig. 1 (b) and (c)). After the heat treatment for 100 h, the V_3B_2 phase nearly disappeared, while the V_3Si phase was newly formed (Fig. 1 (b)). Comparing the microstructures after annealing for 100 h and 200 h, no evident microstructural changes were observed (Fig. 1 (c)). After the heat treatment, V_5SiB_2 was suggested by EBSD (Fig. 1 (b) and (c)) but could not be detected by XRD (Fig. 2). The phase area fractions obtained from the EBSD phase mappings are indicative of the phase volume fractions and will be used as such in this work (Fig. 1 (d)). The phase area fractions after the heat treatment at 1400 °C for 100 h are almost the same as after 200 h (Fig. 1 (d)), which indicates that a duration of 100 h is sufficient for the heat-treated V−5Si−9B alloy to reach the phase equilibrium at this temperature.

W.G. Yang et al., Intermetallics, 151 (2022) 107691
https://doi.org/10.1016/j.intermet.2022.107691

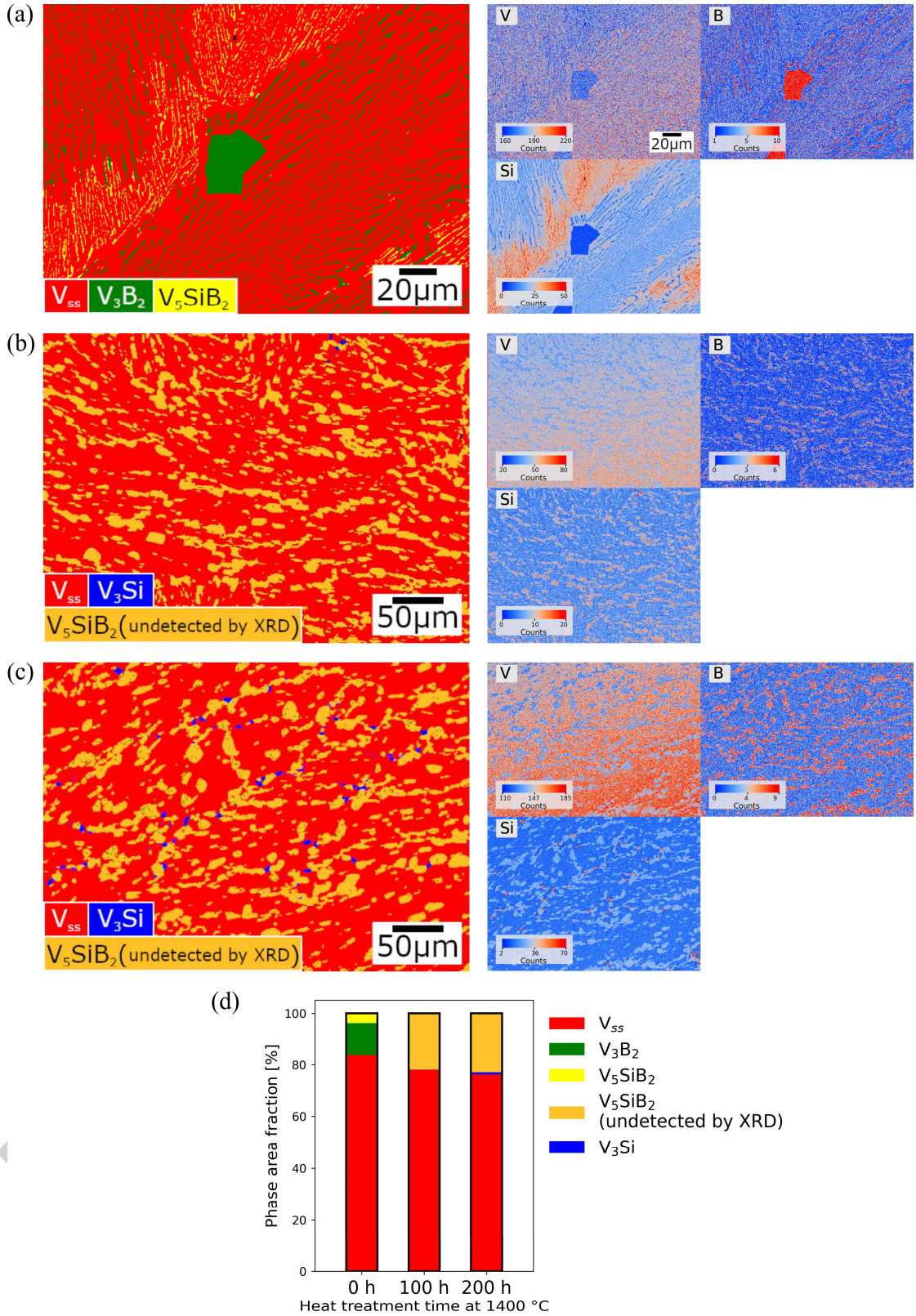

Fig. 1. EBSD phase mappings and EDS elemental mappings of the V−5Si−9B alloy variants: (a) as-cast, (b) heat-treated at 1400 °C for 100 h, and (c) heat-treated at 1400 °C for 200 h. (d) The phase area fractions obtained from the EBSD phase mappings. Phase area fractions are similar after 100 h and 200 h of heat treatment.

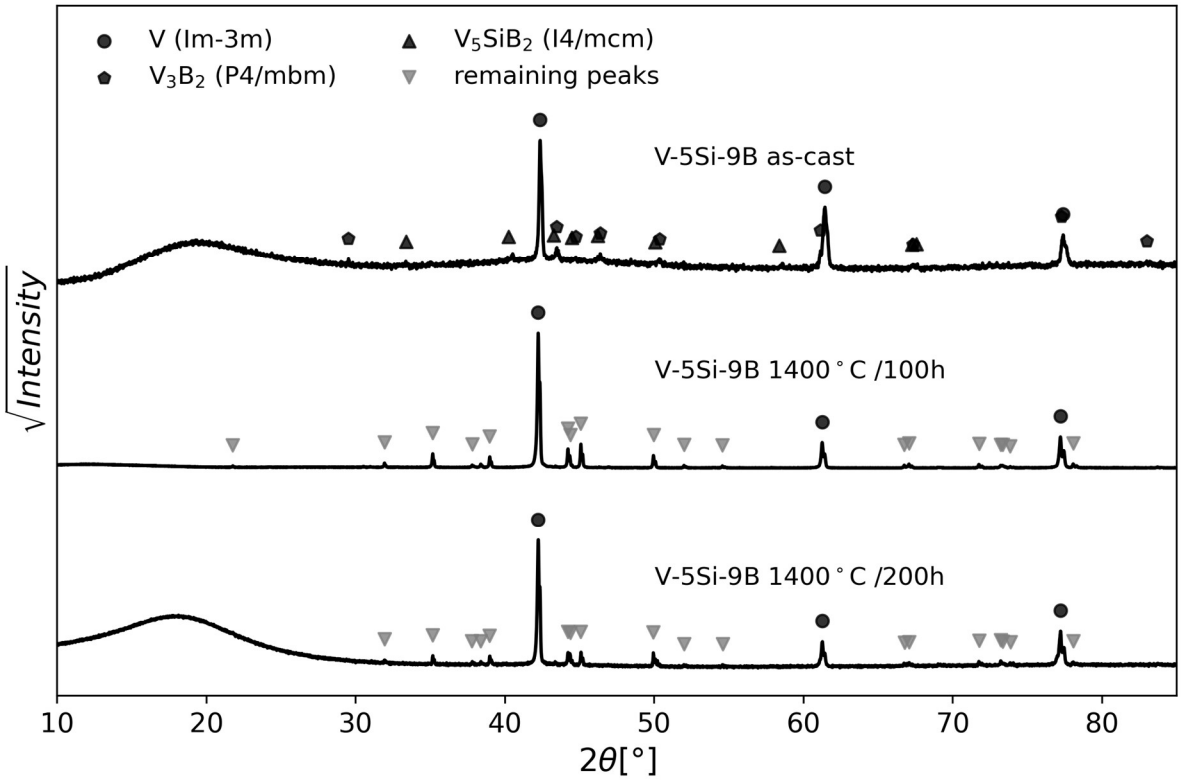

Fig. 2. XRD patterns of the as-cast and heat-treated V−5Si−9B alloys. The fluctuations of the intensity background of the as-cast and heat-treated (1400 °C/ 200 h) alloys at $2\theta \approx 20°$ come from the resin. After the heat treatment at 1400 °C, the V_5SiB_2 phase wasnot confirmed by XRD.

The lattice parameters of the phases in the as-cast and heat-treated alloys are listed in Table 1. The calculated results are reasonable as they resemble the lattice parameters of V_{ss}, V_3B_2 and V_5SiB_2 in the alloys V−6Si−26.5B (1600 °C/24 h) and V−15Si−7.5B (1600 °C/24 h) reported by Nunes et al. [18]. The identified diffraction reflections by the Pawley refinement are marked with different symbols corresponding to different phases in Fig. 2. In the as-cast V−5Si−9B alloy, all diffraction reflections can be explained by the existence of V_{ss}, V_3B_2 and V_5SiB_2 phases (Fig. 2) in agreement with the observed microstructure (Fig. 1 (a)). By contrast, in the XRD patterns of the heat-treated V−5Si−9B alloys (Fig. 2) many unidentified diffraction reflections but none of V_5SiB_2 can be observed, which are marked by grey triangles in Fig. 2. These remaining diffraction reflections most likely represent a new phase having a crystal structure similar to V_5SiB_2 according to the EBSD phase mappings (Fig. 1 (b) and (c)). The V_3Si phases observed with EBSD in the heat-treated V−5Si−9B alloys were not detected by XRD (Fig. 2) due to the low volume fractions of V_3Si indicated by the low area fractions (0.1 % after 100 h and 0.86 % after 200 h) in Fig. 1 (d).

Based on the EDS point measurements shown in Fig. 3, the potentially new phases in alloy V−5Si−9B annealed at 1400 °C for either 100 h or 200 h have B-contents of 31.2 ± 1.0 at% and 29.6 ± 0.9 at%, and 6.5 ± 0.2 at% and 6.6 ± 0.1 at% for Si. Considering the accuracy of the EDS measurement, the measured compositions of those phases in both heat-treated conditions are almost identical. Moreover, despite a different crystal structure compared with that of V_5SiB_2, the measured composition of the new phase in this work is very close to the composition of the V_5SiB_2 phase (V−6.49Si−31.49B) in the phase fields of V_{ss}−V_3Si−V_5SiB_2, V_{ss}−V_3B_2−V_5SiB_2, and VB−V_3B_2−V_5SiB_2 at 1600 °C reported by Nunes et al. [18].

Table 1. The lattice parameters of V_{ss}, V_3B_2 and V_5SiB_2 in the as-cast and heat-treated (1400 °C, 100/200 h) alloys V−5Si−9B calculated by Pawley refinement. The lattice parameters of the phases in the V−6Si−26.5B (1600 °C/ 24 h) and V−15Si−7.5B (1600 °C/ 24 h) alloys [18] are shown for comparison.

alloy	Ref.	V_{ss} (*Im*−3*m*)	V_3Si (*Pm*−3*n*)	V_3B_2 (*P*4/mbm)		V_5SiB_2 (*I*4/*mcm*)	
		a (Å)	*a* (Å)	*a* (Å)	*c* (Å)	*a* (Å)	*c* (Å)
V−5Si−9B (as-cast)	This work	3.019	-	5.732	3.032	5.762	10.740
V−5Si−9B (1400 °C/100 h)	This work	3.024	-	-	-	-	-
V−5Si−9B (1400 °C/200 h)	This work	3.022	-	-	-	-	-
V−6Si−26.5B (1600 °C/ 24 h)	[18]	3.039	-	5.749	3.031	5.785	10.765
V−15Si−7.5B (1600 °C/ 24 h)	[18]	3.037	4.746	-	-	5.785	10.779

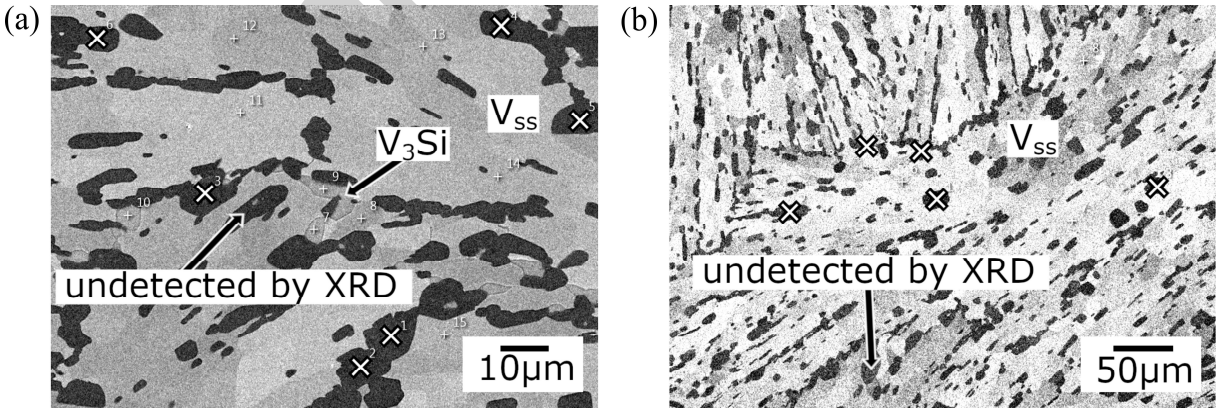

Fig. 3. EDS point measurements of the potentially new phase are marked by 'X' in alloys V−5Si−9B after the heat treatments of (a) 1400 °C/100 h and (b) 1400 °C/200 h.

3.2 *Determination and description of the crystal structure of the new phase*

According to the XRD results and the observed microstructural change after the heat treatments at 1400 °C for 100 h and 200 h, the remaining unidentified diffraction reflections of the heat-treated alloys V−5Si−9B (Fig. 2) indicate the presence of a new phase. To index the remaining diffraction reflections, a primitive tetragonal Bravais lattice (*P*4/*mmm*), which is the base of the space group *I*4/*mcm* (crystal structure of V_5SiB_2), was used by GSAS-II [22]. The indexing can provide a plausible solution with the following lattice parameters $a = 5.768$ Å and $c = 16.800$ Å for the alloy V−5Si−9B (1400 °C/100 h) and $a = 5.767$ Å and $c = 16.791$ Å for the alloy V−5Si−9B (1400 °C/200 h). Compared with the lattice parameters of V_5SiB_2 at 1600 °C [18] shown in Table 1, one has to point out two observations: first, the lattice parameter a of the new phase is almost the same as that of the V_5SiB_2 phase, so that $a_{new} \approx a_{T2}$, second, the lattice parameter c of the new phase is approximately 1.56 times larger than that of the V_5SiB_2 phase, leading to $c_{new} \approx 1.56\ c_{T2}$.

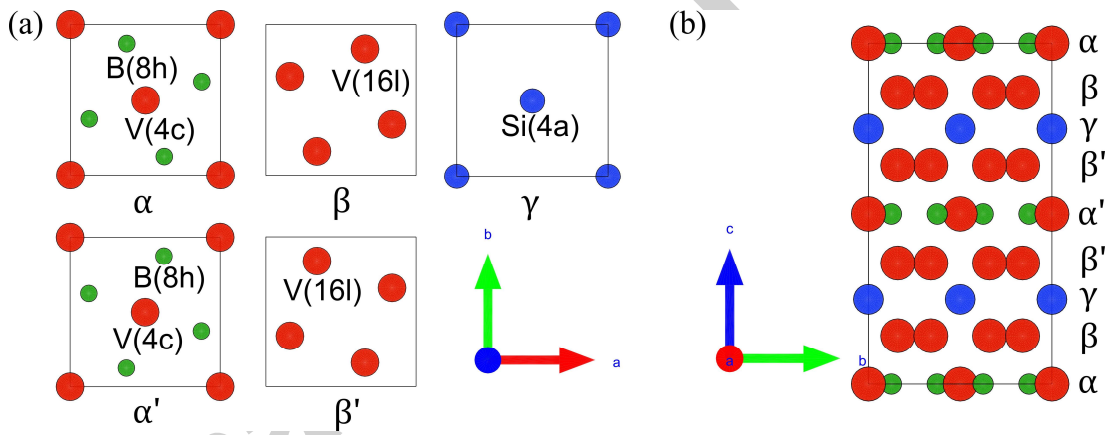

Fig. 4. Atomic arrangements in the crystal structure of V_5SiB_2: (a) atomic layers and (b) stacking sequence along the c-axis.

The first finding $a_{new} \approx a_{T2}$ indicates that the atomic layers and stacking sequence along the *c*-axis in the new phase should be similar to that of V_5SiB_2 to maintain a similar lattice parameter *a*. Examining the crystal structure of V_5SiB_2, atoms are arranged in five different stacking layers along the *c*-axis, as shown in Fig. 4 (a). In the *α*- and *α*′-layers, there are two atom types V1 (4c) and B (8h), while in β- and β′-layers just one atom type V2 (16l) occurs. The γ-layer is solely formed by Si atoms (4a). The stacking sequence of these atomic layers in a conventional unit cell of V_5SiB_2 is ···αβγβ′α′β′γβα··· as shown in Fig. 4 (b), with four atomic layer distances $d_{\alpha-\beta}$, $d_{\alpha'-\beta'}$, $d_{\beta-\gamma}$ and $d_{\beta'-\gamma}$. Thus, to have a stacking sequence similar to V_5SiB_2, the lattice parameter c_{new} of the new phase is defined using the atomic layer distances along the *c*-axis in V_5SiB_2:

$$c_{\text{new}} = N_{\alpha-\beta} \cdot d_{\alpha-\beta} + N_{\alpha'-\beta'} \cdot d_{\alpha'-\beta'} + N_{\beta-\gamma} \cdot d_{\beta-\gamma} + N_{\beta'-\gamma} \cdot d_{\beta'-\gamma}, \quad (1)$$

where $N_{\alpha-\beta}$, $N_{\alpha'-\beta'}$, $N_{\beta-\gamma}$ and $N_{\beta'-\gamma}$ are the numbers of the corresponding atomic layer distances; $d_{\alpha-\beta}$, $d_{\alpha'-\beta'}$, $d_{\beta-\gamma}$ and $d_{\beta'-\gamma}$ were calculated using the calculated atomic Wyckoff sites by Colinet et al. [19] shown in Table 3, resulting in:

$$d_{\alpha-\beta} = d_{\alpha'-\beta'} = 1.4735 \text{ Å and } d_{\beta-\gamma} = d_{\beta'-\gamma} = 1.2173 \text{ Å}$$

Furthermore, the pure V layer β or β′ appears in every other atomic layer as shown in Fig. 4 (b). Thus, the stacking sequences of βαβ and β′α′β′ cause the appearance of two $d_{\alpha-\beta}$ in pairs and two $d_{\alpha'-\beta'}$ in pairs, while the stacking sequence of βγβ′ or β′γβ causes the appearance of $d_{\beta-\gamma}$ and $d_{\beta'-\gamma}$ in pairs, which leads to further conditions:

$$N_{\alpha-\beta} = 2n_1, \quad (2)$$

$$N_{\alpha'-\beta'} = 2n_2, \quad (3)$$

$$N_{\beta-\gamma} = N_{\beta'-\gamma}, \quad (4)$$

$$N_{\beta-\gamma} + N_{\beta'-\gamma} = 2n_3, \quad (5)$$

where n_1, n_2, n_3 are integers. By substituting (2)-(5) in Eq. (1) and using the corresponding interlayer distances, Eq (1) can be simplified to:

$$c_{\text{new}} = 2(n_1 + n_2) \cdot 1.4735\text{Å} + 2n_3 \cdot 1.2173\text{Å}. \quad (6)$$

Based on $c_{\text{new}} \approx 1.56\, c_{T2}$, the optimal solution of $(n_1 + n_2)$ and n_3 for Eq. (6) can be determined to yield a c_{new} as close as possible to $c_{\text{new}} \approx 1.56\, c_{T2}$, with $c_{T2} = 10.763$ Å according to DFT calculations [19]. The optimal solution of $2(n_1 + n_2) = N_{\alpha-\beta} + N_{\alpha'-\beta'} = 8$ and $2n_3 = N_{\beta-\gamma} + N_{\beta'-\gamma} = 4$, leads to $c_{\text{new}} = 16.657$ Å close to the experimentally found value for $c_{\text{new}} \approx 1.56\, c_{T2} = 16.790$ Å. As a consequence, there should be eight distances for $d_{\alpha-\beta}$ or $d_{\alpha'-\beta'}$ and four distances for $d_{\beta-\gamma}$ or $d_{\beta'-\gamma}$ within the conventional unit cell of the new phase, thus increasing the total numbers of layers α&α′ and β&β′ from two and four in the conventional unit cell of V_5SiB_2 to four and six, respectively, in the new phase, while the number of layer γ (two) does not change. All of the considerations mentioned above lead to three possible stacking sequences of the new phase as proposed in Fig. 5. The three models shown in Fig. 5 have the same chemical formula V_8SiB_4, which is close to the measured composition of the new phase (see Section 3.1). After performing the structural relaxation using DFT, their differences in the formation

enthalpies and their lattice parameters are shown in Table 2. Models I and II have similar lattice parameters, which are in good agreement with the measured ones obtained via XRD and differ clearly from the lattice parameters of Model III. Similarly, the formation enthalpy of Model I is the lowest but very close to that of Model II, while Model III exhibits the largest formation enthalpy. Therefore, the optimized crystal structure of Model I after the structural relaxation was further used to simulate the XRD pattern to compare with the remaining diffraction reflections in the V−5Si−9B alloy heat-treated at 1400 °C for 100 h and 200 h. As shown in Fig. 6, all unidentified diffraction reflections of the heat-treated alloys can now be explained by the simulated XRD pattern using the DFT relaxed Model I. Thus, Model I presumably represents the crystal structure of V_8SiB_4. Furthermore, after the Rietveld refinement using GSAS-II [22], the calculated and experimental values of 2θ and intensities for (*hkl*) reflections of V_8SiB_4 of the heat-treated (1400 °C/ 100 h) V−5Si−9B are given in Table A1 (see appendix).

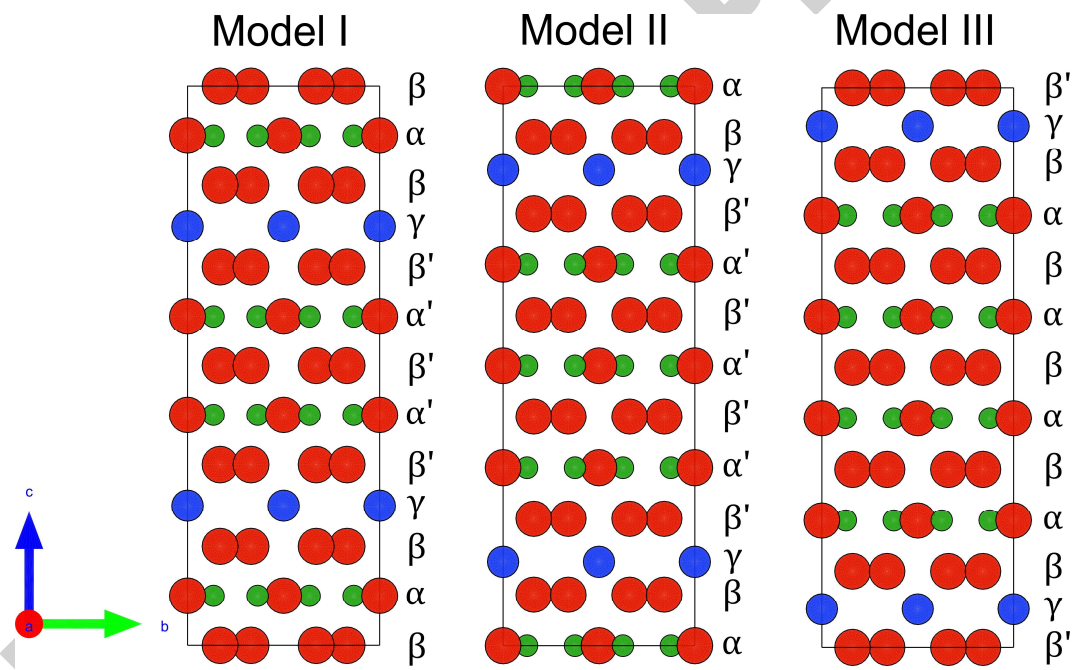

Fig. 5. Possible crystal structures of the new phase with the different atomic layer stacking sequences.

Table 2. DFT-calculated (QE) values of the differences of the enthalpies of formation and lattice parameters for the three different stacking models.

	$\Delta(\Delta_f H)$ (kJ/mol per atom)	Lattice parameters (Å)	
		a	*c*
Model I	0	5.771	16.803
Model II	+0.2	5.770	16.799
Model III	+2.1	5.757	16.835

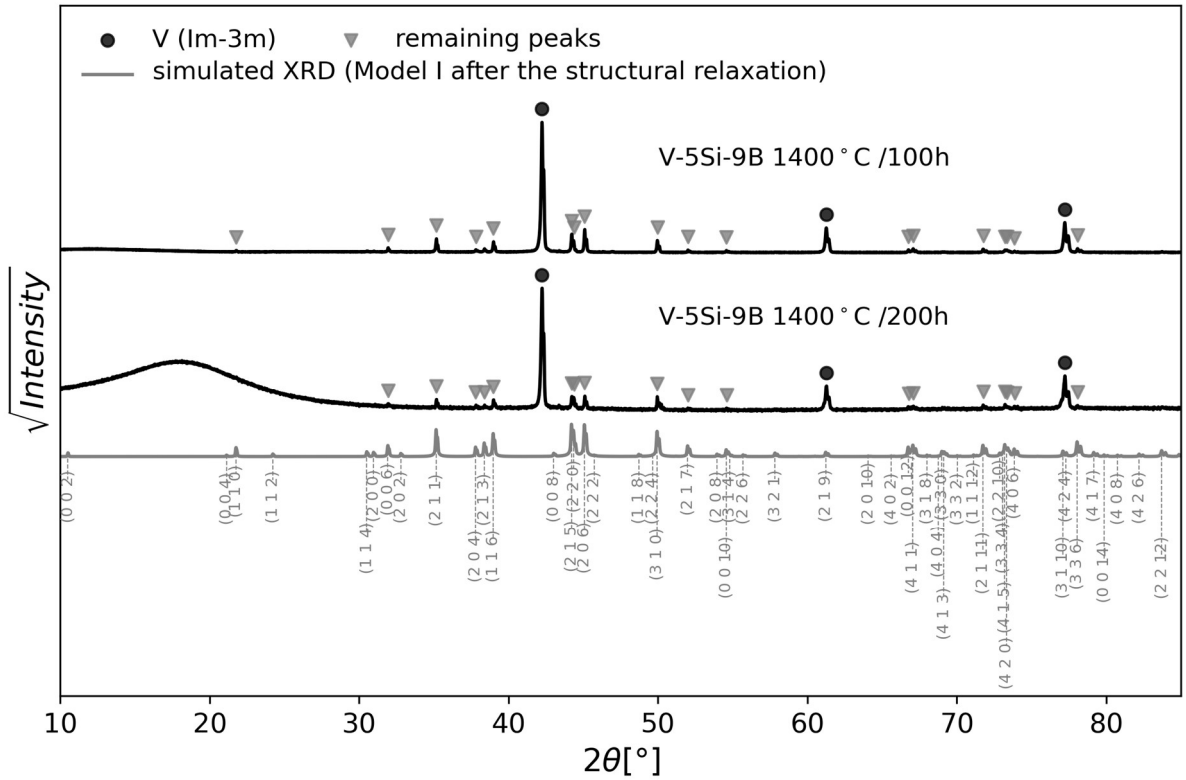

Fig. 6. The simulated XRD pattern (grey curve) of the relaxed Model I agrees very well with the previously unidentified reflections in the heat-treated V−5Si−9B alloys. The fluctuation of the intensity background of the heat-treated (1400 °C/ 200 h) V−5Si−9B at $2\theta \approx 20°$ comes from the resin.

The crystallographic information of the new phase V_8SiB_4 is listed in Table 3. After searching through the AFLOW library of crystallographic prototypes [54,55], the novel V_8SiB_4 phase may represent a new crystallographic prototype. According to the atomic positions after the structural relaxation, the space group *I*4/*mcm* (No. 140) describes the symmetry of V_8SiB_4. Although the space groups of V_5SiB_2 and V_8SiB_4 are the same (Table 3), there are clear differences in the atomic surroundings. The crystal structure of V_8SiB_4 consists of a building block of two halves of V_5SiB_2 from layer α to α' and α' to α (Fig. 4) separated by layers β and β′ (Fig. 7). These extra separating layers β and β′ are formed by V atoms on the Wyckoff position 8h (V3) (Table 3), which then after relaxation slightly change their x-coordinates. In addition to the insertion of V layers, the B and V atoms in the layers α and α' in V_5SiB_2 change their Wyckoff positions in V_8SiB_4 from 8h and 4c to 16l and 8f, respectively, while their coordination spheres also change (Table 3). In the new phase V_8SiB_4, V1 is coordinated linearly along the *c*-axis by Si and V1, quadratically by B and in a quadratic prismatic fashion by V2 and V3. This coordination of Si and V2 atoms resembles a bit the coordination of Al atoms and M atoms in the MAB phases $(CrB_2)_nCrAl$ (n = 1, 2) [56] and Cr_4AlB_4 [57] but else no similarities to MAB phases were found. V2 is coordinated linearly by V3 and

irregularly by the other atoms. For V3 the situation is similar. It is coordinated linearly by V2 and irregularly by the other atoms. Si atoms are located at the center of a twisted quadratic prism made of V2 atoms and are coordinated linearly by V1. B atoms form B−B dumbbells and are the center of a trigonal prism made of V2 and V3. B−B dumbbells can also be found in numerous intermetallic borides like Mo_2FeB_2 [58] or Nb_2OsB_2 [59], while in MAB phases boron usually zigzag chains or more complex boron fragments can be found. In V_5SiB_2 and V_8SiB_4 the V atoms on 16l (V2) and the Si atoms on 4a show similar atomic environments as these atoms are within the building block mentioned above, so it is expected that the lengths of most bonds are similar, too.

Table 3. The crystal structure data of V_8SiB_4 phase compared with V_5SiB_2: The lattice parameters of V_8SiB_4 are the average of the measured values of both heat-treated alloys. The Wyckoff sites of atoms in V_8SiB_4 are based on our DFT calculation. For V_5SiB_2, both the lattice parameters and the Wyckoff sites are from a DFT calculation presented in Ref. [19].

Formula	V_8SiB_4		V_5SiB_2	
Reference	This work		[19]	
Space group	*I*4/*mcm* (No. 140)		*I*4/*mcm* (No. 140)	
Lattice parameters (Å)	a = 5.768	c = 16.796	a = 5.778	c = 10.763
Wyckoff sites	V1	8f (z = 0.0897)	V1	4c
	V2	16l (x = 0.1713, z = 0.1769)	V2	16l (x = 0.1699, z = 0.1369)
	V3	8h (x=0.1773)	V3	-
	Si	4a	Si	4a
	B	16l (x = 0.3872, z = 0.0902)	B	8h (x = 0.3851)

With respect to the bond lengths (Table 4), the V1−B and three of four V2−V2 bond types in V_8SiB_4 are a little longer than those bonds in V_5SiB_2. The B−B, V2−B, V1−V2 and one type of V2−V2 bond in V_8SiB_4 are a bit shorter, though, than the analogous bonds in V_5SiB_2. The V1−Si and V2−Si bond lengths are about the same in both V_8SiB_4 and V_5SiB_2. Despite all the similarities, the V3−B, V1−V1, V1−V3, V2−V3 and V3−V3 bonds are only present in V_8SiB_4, while there is one type of V2−V2 bond, which can only be found in V_5SiB_2. This V2−V2 bond, however, is very similar to the V2−V3 bond in V_8SiB_4 as both bond types are along the *c*-axis and express this similarity also in terms of bond length and bond strength (see also Subsection 3.4, Table 5).

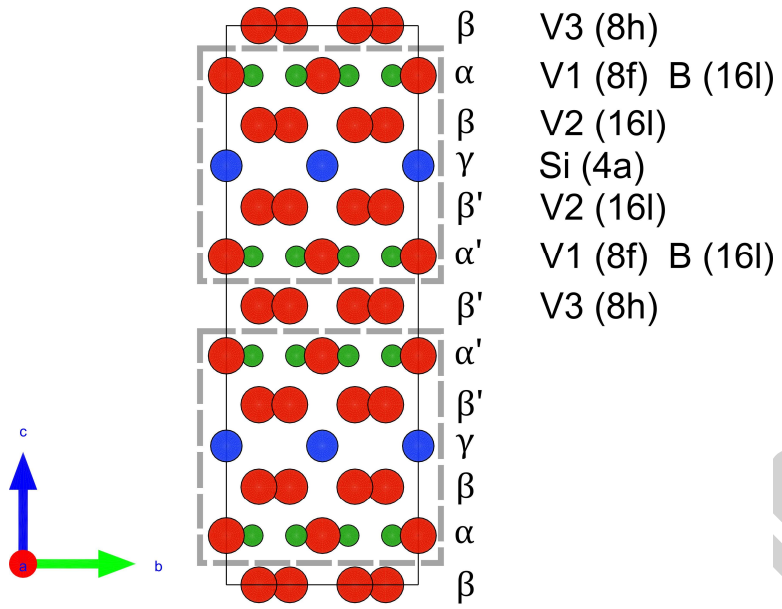

Fig. 7. The stacking sequence of atomic layers along the c-axis and Wyckoff positions of the atomic species in a V_8SiB_4 conventional unit cell. The blocks αβγβ′α′ or α′β′γβα (dashed lines), which are present in V_5SiB_2, are separated by layers β or β′ in V_8SiB_4.

Table 4. Bond types and their distances in V_5SiB_2 and V_8SiB_4.

Bond type	Bond length (Å) V_5SiB_2	Bond length (Å) V_8SiB_4
B–B	1.878	1.841
V1–B	2.322	2.327
V2–B	2.232	2.219
V2–B	2.294	2.286
V3–B	-	2.286
V3–B	-	2.289
V1–Si	2.691	2.693
V2–Si	2.467	2.466
V1–V1	-	3.014
V1–V2	2.602	2.592
V1–V3	-	2.604
V2–V2	2.764	2.772
V2–V2	2.777	2.795
V2–V2	2.947	-
V2–V2	3.034	3.024
V2–V2	3.128	3.153
V2–V3	-	2.973
V3–V3	-	2.894
V3–V3	-	3.004

3.3 *First principles calculation of the lattice parameters and formation enthalpy of V_8SiB_4 and V_5SiB_2*

To ensure the quality of the results of the calculation of the phononic structure, the crystal structure of V_5SiB_2 and V_8SiB_4 were also relaxed with CP2k.

The deviation of the DFT calculated lattice parameters *a* and *c* for both V_8SiB_4 and V_5SiB_2 are within 1 % and therefore in very good agreement with the experimental lattice parameters. The formation enthalpy of V_8SiB_4 calculated with QE and CP2k is −1.4 and −1.8 kJ/mol per atom lower than $\Delta_f H$ of V_5SiB_2, respectively. Therefore, the results gained by QE and CP2k are qualitatively comparable. Furthermore, this means that the formation of V_8SiB_4 seems to be more favorable than the formation of V_5SiB_2. Surprisingly, the V_8SiB_4 has not been reported before, which indicates that it may be unstable under certain conditions compared with the V_5SiB_2. To further confirm the stability of V_8SiB_4 at 0 K, its EDOS, PDOS and chemical bonding and elastic properties were examined and compared with those of V_5SiB_2 in the following section.

3.4 *Electronic structure, phononic density-of-states, chemical bonding and elastic properties of V_8SiB_4 and V_5SiB_2*

In Fig. 8 EDOS of V_5SiB_2 and V_8SiB_4 are presented.

Because of the similar crystal structure of V_5SiB_2 and V_8SiB_4, both EDOSs are very similar, as expected. For both EDOSs, the states range from −11 to −7.5 eV and from −7 to at least +5 eV. The similar shape of the partial EDOSs, especially the V and B EDOS, indicates significant covalent bonding within the crystal structure. Because of the non-vanishing EDOS at the Fermi level, V_5SiB_2 and V_8SiB_4 should be metals. Differences can be found in the shape of the EDOSs, especially in the areas of −11 to −7.5 eV and −7 to −5 eV. The origin of these differences can be assigned to the difference in the crystal structure, such as the additional V plane and the slight shift of the B atoms in the V1−B plane in V_8SiB_4 as the EDOS in these two areas is dominated by the partial EDOS of B and V. At the Fermi level of V_8SiB_4, a small maximum of the EDOS occurs, which might indicate a structural instability.

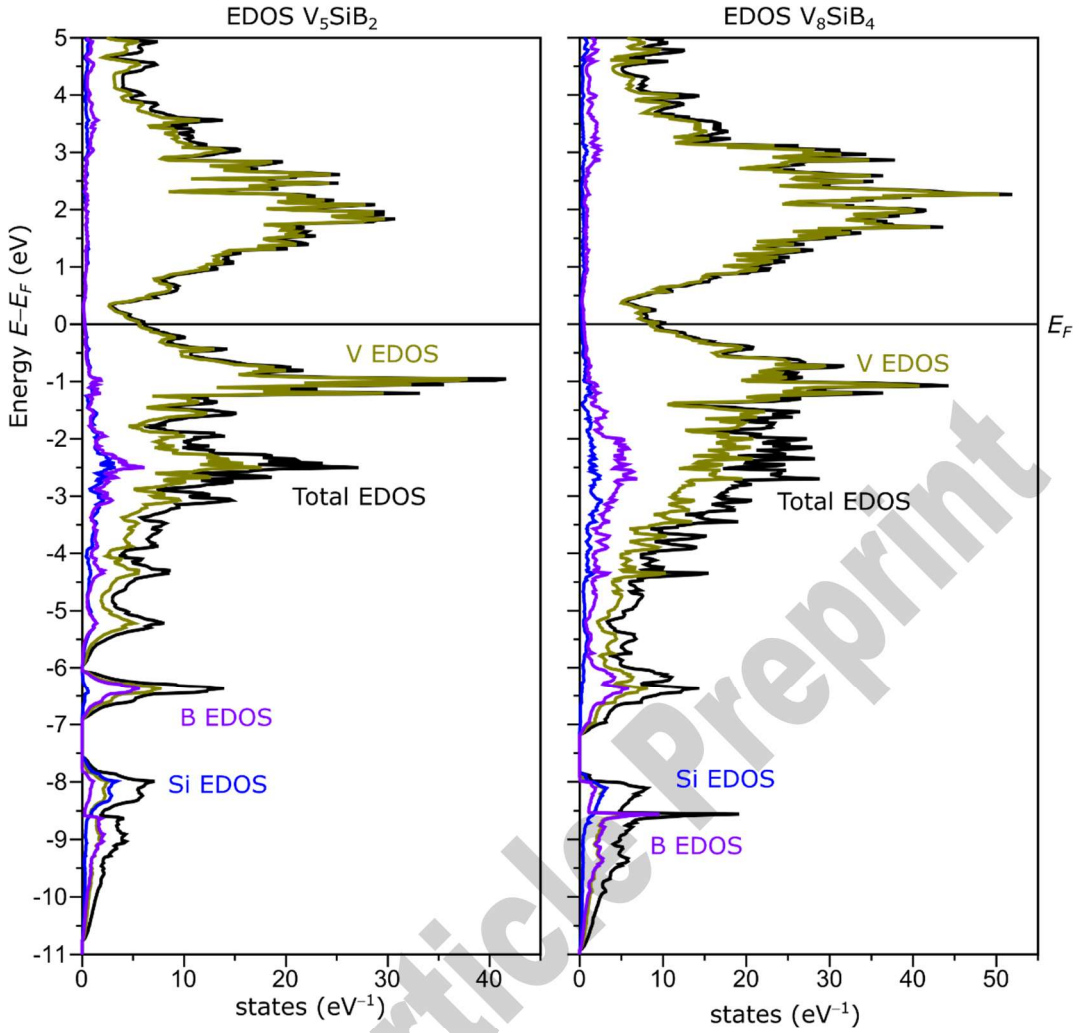

Fig. 8. The EDOSs of V_5SiB_2 (left) and V_8SiB_4 (right) are very similar. The total EDOS is black, while the partial EDOS of V, Si, and B are olive, blue and purple, respectively.

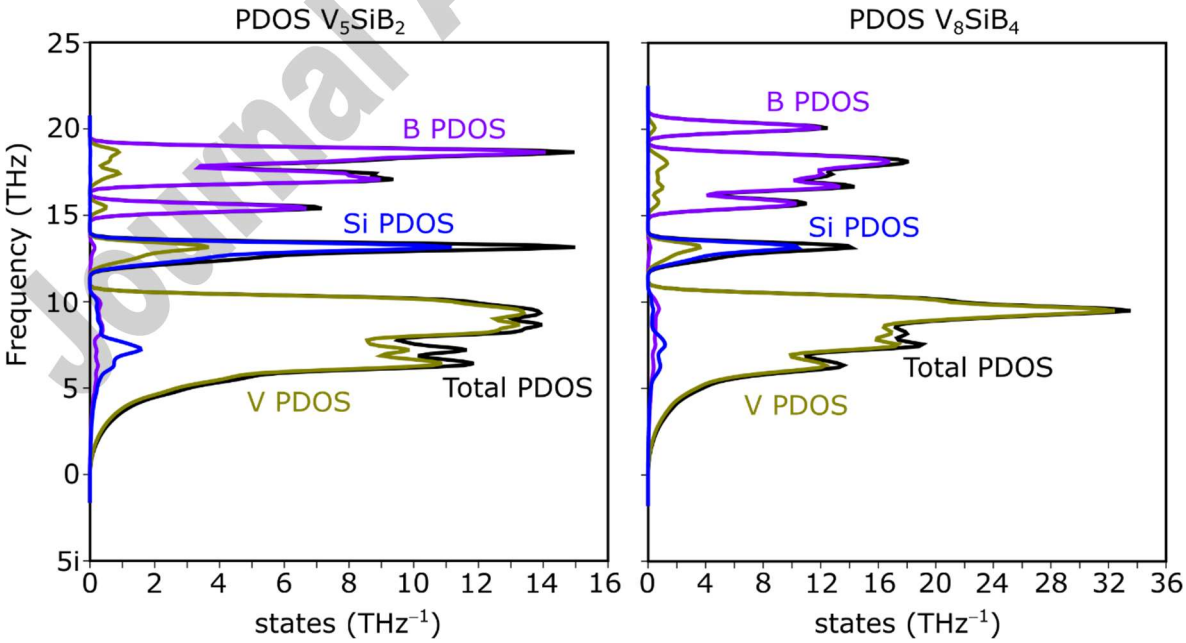

Fig. 9. Both the PDOS of V_5SiB_2 (left) and the PDOS of V_8SiB_4 (right) do not show imaginary frequencies. The total PDOS is black, the partial PDOS of V, Si, and B are olive, blue and purple, respectively.

An indicator for a dynamically and mechanically unstable structure is the presence of imaginary frequencies in the PDOS. The PDOSs of V_5SiB_2 and V_8SiB_4 are shown in Fig. 9.

Again, as the crystal structures are similar, the PDOSs of V_5SiB_2 and V_8SiB_4 do not differ much from each other. From 1 to 11 THz the total PDOSs of both compounds are dominated by V as it is the heaviest atom in the ternary V−Si borides. Between 12 and 14 THz the partial PDOS of Si contributes most to the total PDOS. From 15 to 19 THz the partial PDOS of B is the main contributor, while V contributes less to the total PDOS. The differences in the total PDOSs of V_5SiB_2 and V_8SiB_4 can be found in the areas 8 to 11 THz as well as at 17 THz and 19 to 22 THz, where the total PDOSs are dominated by the partial PDOSs of V and B, respectively. The origin of these differences lies in the differences in the crystal structure as already discussed for the EDOS (Fig. 8). Most importantly, no imaginary frequencies are observed, neither for V_5SiB_2 nor V_8SiB_4, which means that both phases are mechanically and dynamically stable.

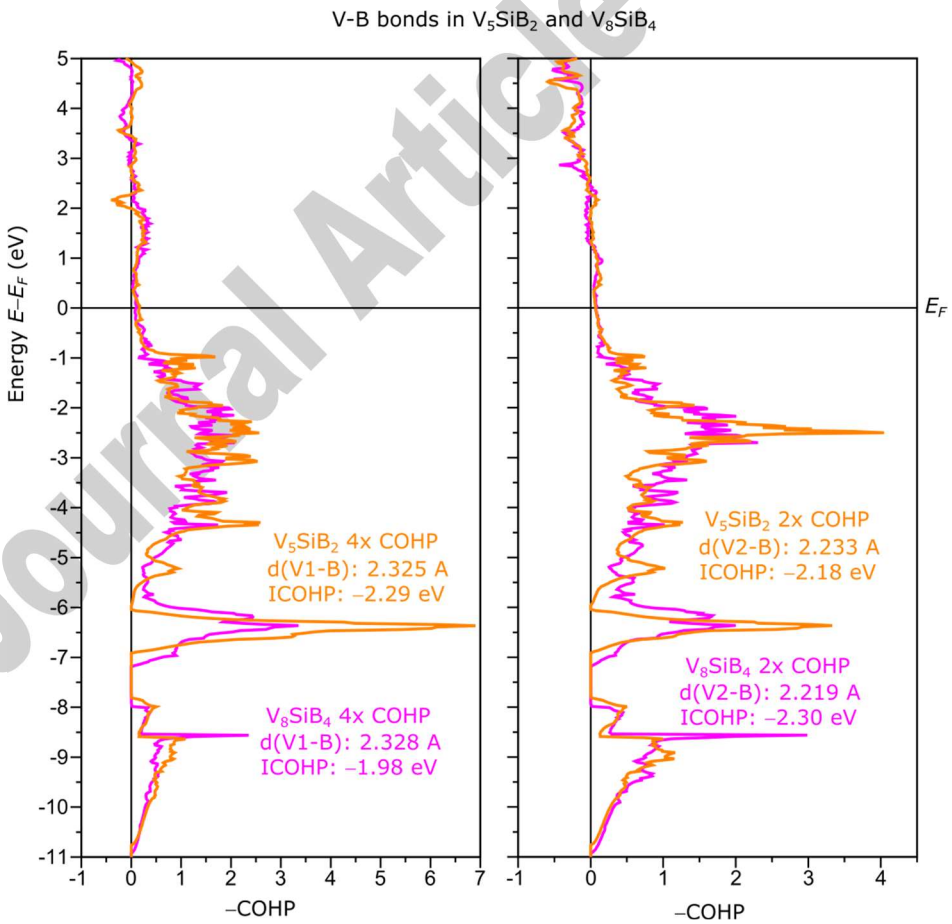

Fig. 10. −COHP-plots of the different V−B bonds in V_5SiB_2 (orange) and V_8SiB_4 (magenta) show the stability of V−B bonds in V_5SiB_2 and V_8SiB_4.

Next, the chemical bonding of selected similar bonds in V_5SiB_2 and V_8SiB_4 will be discussed. First, −COHP-plots of the V−B bonds in these borides are given in Fig. 10.

The atom types V1 and V2 in V_5SiB_2 and V_8SiB_4 are very similar in terms of atomic positions and surroundings and that is why similar −COHP-plots can be expected.

The situation for the V1−B bond is shown on the left side of Fig. 10, while the interactions within the shorter of two types of V2−B bonds is shown on the right side. In general, the V−B bonds in V_5SiB_2 and V_8SiB_4 are very similar. There are bonding interactions present from −11 to −8 eV and from −7 eV to above the Fermi level. At the Fermi level the −COHP is almost zero, which is an indicator for a very stable bond. As the shape of the −COHP is mainly influenced by the EDOS (Fig. 8), the same characteristic differences between V_5SiB_2 and V_8SiB_4 can be seen within the V1−B and V2−B bonds in the regions −11 to −8 eV and −7 to −5.5 eV. The differences in the shape also are the cause for the different ICOHPs. While the V1−B bond in V_5SiB_2 is stronger by −0.31 eV per bond than the same bond in V_8SiB_4, the V2−B bond in V_8SiB_4 is stronger by −0.12 eV per bond than the same bond in V_5SiB_2. The rule of thumb "shorter bonds are stronger bonds" seems to apply in the case of V−B bonds in the borides V_5SiB_2 and V_8SiB_4.

The B−B bonds in V_5SiB_2 and V_8SiB_4 will be discussed next, followed by the discussion of the V3−V3 bonds in V_8SiB_4.

The −COHP plots of the B−B bond (Fig. 11 left) of V_5SiB_2 and V_8SiB_4 are very similar. From −11 to −8 eV there are bonding states. From −7 to −6 eV the states are antibonding. From −6 to −2 eV the bonding interaction is again bonding, while from −2 to −1 eV there are very small antibonding contributions. From −1 eV to the Fermi level non-bonding states are indicating a very stable bonding situation. The B−B bond in V_8SiB_4 is shorter and stronger than the B−B bond in V_5SiB_2 by about 0.038 Å and −0.19 eV, respectively.

In V_8SiB_4 the additional V3 atom takes part in two different types of V3−V3 bonds, one short (2.869 Å) and one long bond (3.005 Å). The −COHP plot is shown in Fig. 11 right. From −11 to −2 eV both bond types are very similar in shape, showing bonding state from −11 to −8 eV and from −7 to −2 eV. From −2 to −1 eV the −COHP of the shorter bond is occupied exclusively with bonding states, while in the longer bond there are small amounts of antibonding and bonding states present. At the Fermi level

only little bonding interactions are found. The shorter V3−V3 bond is also stronger by −0.21 eV.

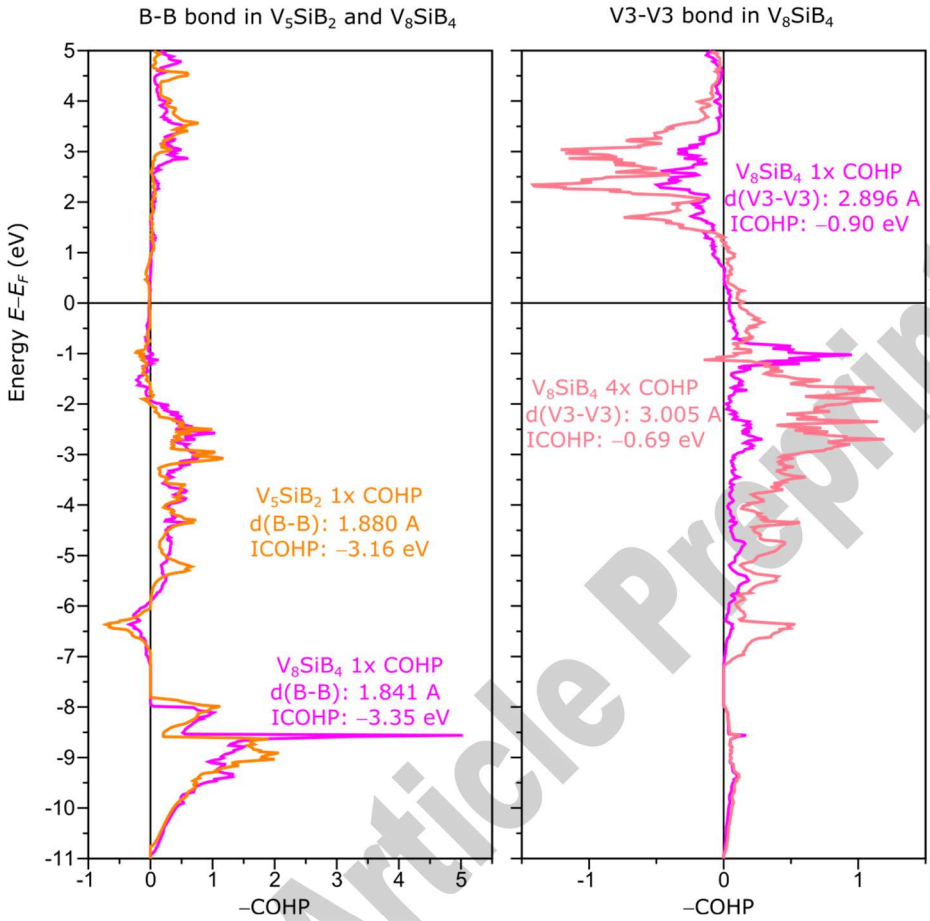

Fig. 11. −COHP-plots of the B−B bonds (left) in V_5SiB_2 (orange) and V_8SiB_4 (magenta) look similar and are stable. −COHP-plots of the short (magenta) and long (pink) V3−V3 bonds (right) in V_8SiB_4 show no sign of instability.

In the as-cast samples no V_8SiB_4 was found. Also, previous synthetic routes [5,18,60] seem not to have led to V_8SiB_4. This means that regardless of the lower formation enthalpy $\Delta_f H$ (Table 6) and the absence of imaginary frequencies in the PDOS (Fig. 9) there must be a reason why V_8SiB_4 seems to be less stable than V_5SiB_2 as it was not found previously. One small hint can already be seen in the EDOS in Fig. 11. The Fermi level lies close to a small maximum of the EDOS, which is a sign of electronic instability. Nonetheless, the maximum does not seem to be dominant and therefore another origin of instability is possible. Fig. 12 shows the −COHP-plot of the V2−V3 bond.

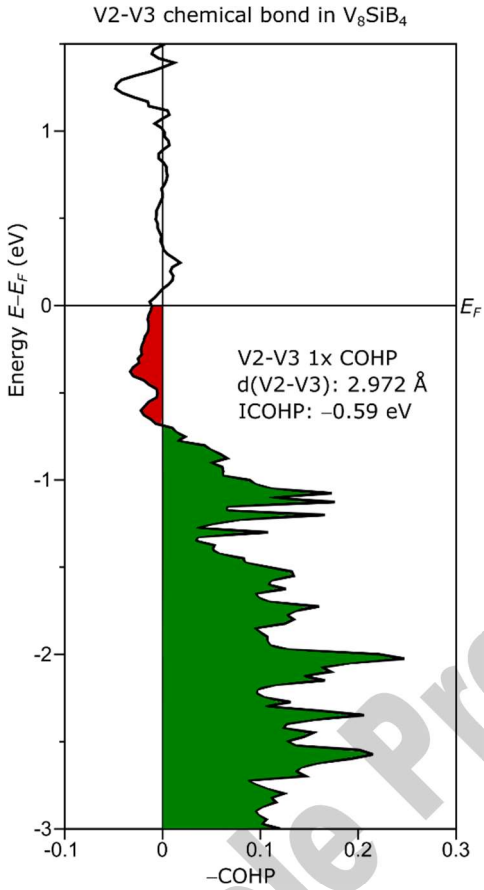

Fig. 12. −COHP-plot of the V2−V3 bond. Near and at the Fermi level antibonding states are occupied, a sign of an unstable chemical bond

The V2−V3 bond is not present in V_5SiB_2 but exists in V_8SiB_4. Near and at the Fermi level, antibonding states are occupied, a clear sign of instability. This unstable chemical bond might explain the instability of V_8SiB_4 at different reaction conditions as in V_5SiB_2 unstable chemical bonding is absent.

To conclude, the chemical bonding strength in terms of ICOHPs of all bonds will be discussed and are shown in Table 5.

Except for the bond types V1−V2, V1−B and V1−Si, all remaining similar bonds in V_8SiB_4 are stronger than the bonds in V_5SiB_2. Overall, the covalent bonding is a bit stronger in V_8SiB_4 (−1.72 eV per bond) than in V_5SiB_2 (−1.69 eV per bond), which indicates that the elastic moduli of V_8SiB_4 are a bit higher than those of V_5SiB_2 similar as reported for the elastic moduli of Mo_2TMB_2 (TM = Zr, Hf) [61] and A_2MB_2 borides (A = Nb, Ta; M = Fe, Ru, Os) [62].

Table 5. Bond types and their ICOHP per bond in V_5SiB_2 and V_8SiB_4

Bond type (Number in unit cell)	ICOHP in V_5SiB_2 (eV)	ICOHP in V_8SiB_4 (eV)
V1−V2 (32x)	−1.81	−1.79
V1−Si (8x)	−1.39	−1.24
V2−Si (32x)	−1.90	−2.00
V2−V2 (8x)	−1.44	−1.55
V2−V2 (8x)	−1.11	−1.51
V2−V2 (4x)	−0.53	
V2−V2 (16x)	−0.66	−0.75
V2−V2 (8x)	−0.54	−0.87
V1−B (16x/32x)	−2.29	−1.98
V2−B, short (16x)	−2.18	−2.30
V2−B, long (16x)	−2.08	−2.22
B−B (4x/8x)	−3.16	−3.35
V1−V1 (4x)		−0.85
V1−V3 (32x)		−1.73
V2−V3 (16x)		−0.59
V3−B, short (16x)		−2.21
V3−B, long (16x)		−2.04
V3−V3, short (4x)		−0.90
V3−V3, long (8x)		−0.69
Total ICOHP per bond	−1.69	−1.72

As expected according to our DFT calculations, the bulk, shear and Young's moduli as well as the Vickers hardness of V_8SiB_4 are slightly higher than the corresponding values of V_5SiB_2 (Table 6) because of the stronger chemical bonding situation in V_8SiB_4 (Table 5). Especially, but not limited to, the V−B, V−Si and V−V bonds seem to contribute to higher elastic moduli of V_8SiB_4 compared with V_5SiB_2. The elastic constants C_{ij} of V_8SiB_4 can be found in Table A2 (see appendix).

Table 6. Bulk modulus *B*, shear modulus *G*, Young's modulus *Y* and Vickers hardness H_V of V_5SiB_2 [63]and V_8SiB_4.

Compound	*B* (GPa)	*G* (GPa)	*Y* (GPa)	H_V (GPa)
V_8SiB_4	239	193	456	30
V_5SiB_2	230	186	439	29

4 Summary

A new ternary phase V_8SiB_4 was found in the V−Si−B system after annealing, while the V_5SiB_2 (T2) phase was not observed in heat-treated (1400 °C, 100/200 h) V−5Si−9B alloys. Using the crystal similarity of the new ternary phase with V_5SiB_2 (T2) indicated by the X-ray diffraction (XRD) results, we determined the crystal structure of V_8SiB_4 by performing density functional theory (DFT) calculations. To further examine the stability of V_8SiB_4 at 0 K, the electronic density-of-states (EDOS) and phononic density-of-states (PDOS) were calculated and the chemical bonding and elastic properties for both V_5SiB_2 and V_8SiB_4 were investigated. The results of the DFT calculation can be summarized as:

1. The EDOSs of V_5SiB_2 and V_8SiB_4 are very similar. A small peak of the EDOS close to the Fermi level of the V_8SiB_4 might indicate a structural instability.

2. The PDOSs of V_5SiB_2 and V_8SiB_4 do not show imaginary frequencies indicating their dynamical and mechanical stability.

3. The −COHP-plot of the V2−V3 bond in V_8SiB_4 shows antibonding states near and at the Fermi level indicating instability.

Acknowledgments

This work was supported by the Deutsche Forschungsgemeinschaft (DFG), Germany, project number 410338871. The authors would like to thank C. Thomas (PGI−5, FZ Jülich) for providing access to the arc-melter, Dr. W. Behr (ZEA−1, FZ Jülich) and T. Koppitz (ZEA−1, FZ Jülich) for their assistance in heat treatment, Dr. E. Wessel (IEK−2, FZ Jülich) and Dr. D. Grüner (IEK−2, FZ Jülich) for their assistance in SEM investigation as well as EBSD and EDS measurements. R.T. thanks the URZ OVGU Magdeburg for calculation power and time. Financial support of the Methodisch-Diagnostisches Zentrum Werkstoffprüfung (MDZWP) e.V., Magdeburg, Germany is greatly acknowledged.

W.G. Yang et al., Intermetallics, 151 (2022) 107691
https://doi.org/10.1016/j.intermet.2022.107691

Appendix

Table A1. Calculated and experimental values of 2θ and intensities for (*hkl*) reflections of V_8SiB_4 in the heat-treated (1400 °C/ 100 h) V−5Si−9B from the Rietveld refinement. The subscripts Cal, Obs and bg represent calculated, observed and background values, respectively. The reflections marked with "*" overlap with other phases being present in the alloy investigated.

Reflection (*hkl*)	$2\theta_{Cal}$ (°)	$2\theta_{Obs}$ (°)	I_{Cal}/I_{bg} (-)	I_{Obs}/I_{bg} (-)	Reflection (*hkl*)	$2\theta_{Cal}$ (°)	$2\theta_{Obs}$ (°)	I_{Cal}/I_{bg} (-)	I_{Obs}/I_{bg} (-)
0 0 2	10.511	-	1.025	-	2 1 9 *	61.234	-	-	-
0 0 4	21.124	-	1.007	-	2 0 10	64.087	-	1.002	-
1 1 0	21.760	21.771	1.125	1.083	4 0 2	65.627	65.600	1.003	1.010
1 1 2	24.226	24.226	1.016	1.024	0 0 12	66.755	66.755	1.146	1.163
1 1 4	30.515	30.529	1.044	1.048	4 1 1	67.069	67.070	1.202	1.232
2 0 0	30.970	30.975	1.035	1.041	3 1 8	68.014	68.002	1.007	1.016
0 0 6	31.925	31.934	1.179	1.252	4 0 4	68.764	-	1.002	-
2 0 2	32.794	32.800	1.021	1.027	3 3 0	69.013	69.014	1.051	1.036
2 1 1	35.157	35.164	1.938	1.909	4 1 3	69.146	69.132	1.044	1.033
2 0 4	37.798	37.803	1.137	1.132	3 3 2	70.041	-	1.004	-
2 1 3	38.376	38.381	1.266	1.190	1 1 12	71.135	-	1.008	-
1 1 6	38.975	38.985	1.712	1.680	2 1 11	71.757	71.745	1.198	1.201
0 0 8	43.027	43.016	1.050	1.054	2 2 10	72.882	72.900	1.027	1.030
2 1 5	44.219	44.224	2.351	2.304	3 3 4 *	73.089	-	-	-
2 2 0 *	44.373	-	-	-	4 1 5	73.219	73.228	1.218	1.146
2 0 6	45.081	45.090	2.337	2.746	4 2 0 *	73.332	-	-	-
2 2 2	45.734	-	1.009	-	4 0 6	73.852	73.845	1.096	1.065
1 1 8	48.723	48.740	1.013	1.018	3 1 10 *	77.114	-	-	-
2 2 4	49.644	49.659	1.010	1.019	4 2 4 *	77.318	-	-	-
3 1 0	49.948	49.948	1.875	1.826	3 3 6	78.066	78.073	1.331	1.226
2 1 7	51.991	51.997	1.175	1.139	4 1 7	79.176	79.203	1.037	1.021
2 0 8	53.958	53.953	1.015	1.019	0 0 14	79.862	-	1.010	-
0 0 10	54.572	54.570	1.081	1.116	4 0 8	80.771	-	1.007	-
3 1 4 *	54.816	-	-	-	4 2 6	82.216	82.209	1.016	1.020
2 2 6	55.705	55.739	1.009	1.015	2 2 12	83.724	83.733	1.063	1.050
3 2 1	57.840	57.853	1.028	1.024					

Table A2. Elastic constants *Cij* of V_8SiB_4 in GPa.

ij =	1	2	3	4	5	6
1	511.03	91.00	126.23	0	0	0
2	91.00	511.03	126.23	0	0	0
3	126.24	126.24	447.28	0	0	0
4	0	0	0	207.46	0	0
5	0	0	0	0	207.46	0
6	0	0	0	0	0	178.71

*For the C_{ij} of V_5SiB_2 we refer to the Supporting Information of Touzani et al. [63].

References

[1] J.A. Lemberg, R.O. Ritchie, Mo−Si−B Alloys for Ultrahigh-Temperature Structural Applications, Advanced Materials. 24 (2012) 3445–3480. https://doi.org/10.1002/adma.201200764.

[2] B.P. Bewlay, M.R. Jackson, P.R. Subramanian, J.-C. Zhao, A review of very-high-temperature Nb−silicide−based composites, Metall and Mat Trans A. 34 (2003) 2043–2052. https://doi.org/10.1007/s11661-003-0269-8.

[3] F.A. Rioult, S.D. Imhoff, R. Sakidja, J.H. Perepezko, Transient oxidation of Mo–Si–B alloys: Effect of the microstructure size scale, Acta Materialia. 57 (2009) 4600–4613. https://doi.org/10.1016/j.actamat.2009.06.036.

[4] G. Hasemann, I. Bogomol, D. Schliephake, P.I. Loboda, M. Krüger, Microstructure and creep properties of a near-eutectic directionally solidified multiphase Mo–Si–B alloy, Intermetallics. 48 (2014) 28–33. https://doi.org/10.1016/j.intermet.2013.11.022.

[5] M. Krüger, High temperature compression strength and oxidation of a V−9Si−13B alloy, Scripta Materialia. 121 (2016) 75–78. https://doi.org/10.1016/j.scriptamat.2016.04.042.

[6] M. Krüger, V. Bolbut, F. Gang, G. Hasemann, Microstructure Variations and Creep Properties of Novel High Temperature V−Si−B Materials, JOM. 68 (2016) 2811–2816. https://doi.org/10.1007/s11837-016-2096-6.

[7] H. Nowotny, F. Benesovsky, E. Rudy, A. Wittmann, Aufbau und Zunderverhalten von Niob−Bor−Silicium−Legierungen, Monatshefte für Chemie. 91 (1960) 975–990. https://doi.org/10.1007/BF00929565.

[8] C.A. Nunes, D.M. Pinto Júnior, G.C. Coelho, P.A. Suzuki, A.A.A.P. da Silva, R.B. Tomasiello, Isothermal Section of the Nb−Si−B System at 1700 °C in the Nb−$NbSi_2$−NbB_2 Region, J. Phase Equilib. Diffus. 32 (2011) 92–96. https://doi.org/10.1007/s11669-010-9846-x.

[9] P.B. Fernandes, Avaliação experimental e modelagem termodinâmica do Sistema Ta−Si−B na Região Rica em Tântalo, Doutorado em Materiais Metálicos, Cerâmicos e Poliméricos, Universidade de São Paulo, 2009. https://doi.org/10.11606/T.97.2009.tde-24102012-122212.

[10] H. Nowotny, E. Piegger, R. Kieffer, F. Benesovsky, Das Dreistoffsystem: Chrom−Silizium−Bor: Mit 4 Abbildungen, Monatshefte für Chemie. 89 (1958) 611–617. https://doi.org/10.1007/BF00900988.

[11] H. Nowotny, E. Dimakopoulou, H. Kudielka, Untersuchungen in den Dreistoffsystemen: Molybdän−Silizium−Bor, Wolfram−Silizium−Bor und in dem System: VSi_2−$TaSi_2$, Monatshefte Für Chemie Und Verwandte Teile Anderer Wissenschaften. 88 (1957) 180–192.

[12] S.-H. Ha, K. Yoshimi, K. Maruyama, R. Tu, T. Goto, Compositional regions of single phases at 1800 °C in Mo-rich Mo–Si–B ternary system, Materials Science and Engineering: A. 552 (2012) 179–188. https://doi.org/10.1016/j.msea.2012.05.028.

[13] P. Böttcher, Th. Doert, Ch. Druska, S. Bradtmöller, Investigations on compounds with Cr5B3 and In5Bi3 structure types, Journal of Alloys and Compounds. 246 (1997) 209–215. https://doi.org/10.1016/S0925-8388(96)02455-3.

[14] T.T. Dorini, B.X. de Freitas, P.P. Ferreira, N. Chaia, P.A. Suzuki, J.-M. Joubert, C.A. Nunes, G.C. Coelho, L.T.F. Eleno, T2 phase site occupancies in the Cr–Si–B system: a combined synchroton-XRD/first-principles study, Scripta Materialia. 199 (2021) 113854. https://doi.org/10.1016/j.scriptamat.2021.113854.

[15] B. Aronsson, The crystal structure of Mo_5Si_3 and W_5Si_3, Acta Chemica Scandinavica. 9 (1955) 1107–1110.

[16] E. Parthé, B. Lux, H. Nowotny, Der Aufbau der Silizide M_5Si_3, Monatshefte für Chemie. 86 (1955) 859–867. https://doi.org/10.1007/BF00902575.

[17] J.-M. Joubert, C. Colinet, G. Rodrigues, P.A. Suzuki, C.A. Nunes, G.C. Coelho, J.-C. Tedenac, The T2 phase in the Nb–Si–B system studied by ab initio calculations and synchrotron X-ray diffraction, Journal of Solid State Chemistry. 190 (2012) 111–117. https://doi.org/10.1016/j.jssc.2012.02.009.

[18] C.A. Nunes, B.B. de Lima, G.C. Coelho, P.A. Suzuki, Isothermal Section of the V−Si−B System at 1600 °C in the V−VSi_2−VB Region, Journal of Phase Equilibria and Diffusion. 30 (2009) 345–350. https://doi.org/10.1007/s11669-009-9533-y.

[19] C. Colinet, J.-C. Tedenac, First principles calculations of the stability of the T2 and $D8_8$ phases in the V–Si–B system, Intermetallics. 50 (2014) 108–116. https://doi.org/10.1016/j.intermet.2014.02.008.

[20] W.J. Lehmann, I. Shapiro, Isotopic Composition of Boron and its Atomic Weight, Nature. 183 (1959) 1324–1324. https://doi.org/10.1038/1831324a0.

[21] J.A. Bearden, X-Ray Wavelengths, Rev. Mod. Phys. 39 (1967) 78–124. https://doi.org/10.1103/RevModPhys.39.78.

[22] B.H. Toby, R.B. Von Dreele, GSAS-II: the genesis of a modern open-source all purpose crystallography software package, Journal of Applied Crystallography. 46 (2013) 544–549. https://doi.org/10.1107/S0021889813003531.

[23] G.S. Pawley, Unit-cell refinement from powder diffraction scans, Journal of Applied Crystallography. 14 (1981) 357–361. https://doi.org/10.1107/S0021889881009618.

[24] A. Belsky, M. Hellenbrandt, V.L. Karen, P. Luksch, New developments in the Inorganic Crystal Structure Database (ICSD): accessibility in support of materials research and design, Acta Cryst B. 58 (2002) 364–369. https://doi.org/10.1107/S0108768102006948.

[25] H. Kohlmann, C. Hein, R. Kautenburger, T.C. Hansen, C. Ritter, S. Doyle, Crystal structure of monoclinic samarium and cubic europium sesquioxides and bound coherent neutron scattering lengths of the isotopes 154Sm and 153Eu, Zeitschrift Fuer Kristallographie-Crystalline Materials. 231 (2016) 517–523.

[26] J.-L. Staudenmann, The electron charge distribution in V_3Si, Solid State Communications. 26 (1978) 461–468. https://doi.org/10.1016/0038-1098(78)91290-5.

[27] A.B. Riabov, V.A. Yartys, B.C. Hauback, P.W. Guegan, G. Wiesinger, I.R. Harris, Hydrogenation behaviour, neutron diffraction studies and microstructural characterisation of boron oxide-doped Zr–V alloys, Journal of Alloys and Compounds. 293–295 (1999) 93–100. https://doi.org/10.1016/S0925-8388(99)00306-0.

[28] H. Kudielka, H. Nowotny, G. Findeisen, Untersuchungen in den Systemen: V−B, Nb−B, V−B−Si und Ta−B−Si, Monatshefte für Chemie. 88 (1958) 1048–1055. https://doi.org/10.1007/BF00906084.

[29] P. Giannozzi, S. Baroni, N. Bonini, M. Calandra, R. Car, C. Cavazzoni, D. Ceresoli, G.L. Chiarotti, M. Cococcioni, I. Dabo, A.D. Corso, S. de Gironcoli, S. Fabris, G. Fratesi, R. Gebauer, U. Gerstmann, C. Gougoussis, A. Kokalj, M. Lazzeri, L. Martin-Samos, N. Marzari, F. Mauri, R. Mazzarello, S. Paolini, A. Pasquarello, L. Paulatto, C. Sbraccia, S. Scandolo, G. Sclauzero, A.P. Seitsonen, A. Smogunov, P. Umari, R.M. Wentzcovitch, QUANTUM ESPRESSO: a modular and open-source software project for quantum simulations of materials, J. Phys.: Condens. Matter. 21 (2009) 395502. https://doi.org/10.1088/0953-8984/21/39/395502.

[30] P. Giannozzi, O. Andreussi, T. Brumme, O. Bunau, M.B. Nardelli, M. Calandra, R. Car, C. Cavazzoni, D. Ceresoli, M. Cococcioni, N. Colonna, I. Carnimeo, A.D. Corso, S. de Gironcoli, P. Delugas, R.A. DiStasio, A. Ferretti, A. Floris, G. Fratesi, G. Fugallo, R. Gebauer, U. Gerstmann, F. Giustino, T. Gorni, J. Jia, M. Kawamura, H.-Y. Ko, A. Kokalj, E. Küçükbenli, M. Lazzeri, M. Marsili, N. Marzari, F. Mauri, N.L. Nguyen, H.-V. Nguyen, A. Otero-de-la-Roza, L. Paulatto, S. Poncé, D. Rocca, R. Sabatini, B. Santra, M. Schlipf, A.P. Seitsonen, A. Smogunov, I. Timrov, T. Thonhauser, P. Umari, N. Vast, X. Wu, S. Baroni, Advanced capabilities for materials modelling with Quantum ESPRESSO, J. Phys.: Condens. Matter. 29 (2017) 465901. https://doi.org/10.1088/1361-648X/aa8f79.

[31] P.E. Blöchl, Projector augmented-wave method, Phys. Rev. B. 50 (1994) 17953–17979. https://doi.org/10.1103/PhysRevB.50.17953.

[32] A. Dal Corso, Pseudopotentials periodic table: From H to Pu, Computational Materials Science. 95 (2014) 337–350. https://doi.org/10.1016/j.commatsci.2014.07.043.

[33] N. Marzari, D. Vanderbilt, A. De Vita, M.C. Payne, Thermal Contraction and Disordering of the Al(110) Surface, Phys. Rev. Lett. 82 (1999) 3296–3299. https://doi.org/10.1103/PhysRevLett.82.3296.

[34] H.J. Monkhorst, J.D. Pack, Special points for Brillouin-zone integrations, Phys. Rev. B. 13 (1976) 5188–5192. https://doi.org/10.1103/PhysRevB.13.5188.

[35] J.P. Perdew, K. Burke, M. Ernzerhof, Generalized Gradient Approximation Made Simple, Phys. Rev. Lett. 77 (1996) 3865–3868. https://doi.org/10.1103/PhysRevLett.77.3865.

[36] Welcome to Thermo_pw, Welcome to Thermo_pw. (n.d.). https://dalcorso.github.io/thermo_pw/ (accessed September 19, 2021).

[37] W. Voigt, Lehrbuch der Kristallphysik (Textbook of crystal physics), BG Teubner, Leipzig Und Berlin. (1928).

[38] A. Reuss, Berechnung der Fließgrenze von Mischkristallen auf Grund der Plastizitätsbedingung für Einkristalle ., ZAMM - Journal of Applied Mathematics and Mechanics / Zeitschrift Für Angewandte Mathematik Und Mechanik. 9 (1929) 49–58. https://doi.org/10.1002/zamm.19290090104.

[39] R. Hill, The Elastic Behaviour of a Crystalline Aggregate, Proc. Phys. Soc. A. 65 (1952) 349–354. https://doi.org/10.1088/0370-1298/65/5/307.

[40] Y. Tian, B. Xu, Z. Zhao, Microscopic theory of hardness and design of novel superhard crystals, International Journal of Refractory Metals and Hard Materials. 33 (2012) 93–106. https://doi.org/10.1016/j.ijrmhm.2012.02.021.

[41] J. VandeVondele, M. Krack, F. Mohamed, M. Parrinello, T. Chassaing, J. Hutter, Quickstep: Fast and accurate density functional calculations using a mixed Gaussian and plane waves approach, Computer Physics Communications. 167 (2005) 103–128. https://doi.org/10.1016/j.cpc.2004.12.014.

[42] J. Hutter, M. Iannuzzi, F. Schiffmann, J. VandeVondele, cp2k: atomistic simulations of condensed matter systems, WIREs Computational Molecular Science. 4 (2014) 15–25. https://doi.org/10.1002/wcms.1159.

[43] A. Togo, I. Tanaka, First principles phonon calculations in materials science, Scripta Materialia. 108 (2015) 1–5. https://doi.org/10.1016/j.scriptamat.2015.07.021.

[44] B.G. LIPPERT, J.H. and M. PARRINELLO, A hybrid Gaussian and plane wave density functional scheme, Molecular Physics. 92 (1997) 477–488. https://doi.org/10.1080/002689797170220.

[45] J. VandeVondele, J. Hutter, Gaussian basis sets for accurate calculations on molecular systems in gas and condensed phases, J. Chem. Phys. 127 (2007) 114105. https://doi.org/10.1063/1.2770708.

[46] S. Goedecker, M. Teter, J. Hutter, Separable dual-space Gaussian pseudopotentials, Phys. Rev. B. 54 (1996) 1703–1710. https://doi.org/10.1103/PhysRevB.54.1703.

[47] C. Hartwigsen, S. Goedecker, J. Hutter, Relativistic separable dual-space Gaussian pseudopotentials from H to Rn, Phys. Rev. B. 58 (1998) 3641–3662. https://doi.org/10.1103/PhysRevB.58.3641.

[48] M. Krack, Pseudopotentials for H to Kr optimized for gradient-corrected exchange-correlation functionals, Theor Chem Acc. 114 (2005) 145–152. https://doi.org/10.1007/s00214-005-0655-y.

[49] O.K. Andersen, H.L. Skriver, H. Nohl, B. Johansson, Electronic structure of transition metal compounds; ground-state properties of the 3d-monoxides in the atomic sphere approximation, Pure and Applied Chemistry. 52 (1980) 93–118. https://doi.org/10.1351/pac198052010093.

[50] O.K. Andersen, O. Jepsen, Explicit, First-Principles Tight-Binding Theory, Phys. Rev. Lett. 53 (1984) 2571–2574. https://doi.org/10.1103/PhysRevLett.53.2571.

[51] O. Jepsen, O.K. Andersen, The STUTTGART TB-LMTO-ASA program., (n.d.). https://www2.fkf.mpg.de/andersen/LMTODOC/LMTODOC.html (accessed September 19, 2021).

[52] J.P. Perdew, J.A. Chevary, S.H. Vosko, K.A. Jackson, M.R. Pederson, D.J. Singh, C. Fiolhais, Atoms, molecules, solids, and surfaces: Applications of the generalized gradient approximation for exchange and correlation, Phys. Rev. B. 46 (1992) 6671–6687. https://doi.org/10.1103/PhysRevB.46.6671.

[53] R. Dronskowski, P.E. Bloechl, Crystal orbital Hamilton populations (COHP): energy-resolved visualization of chemical bonding in solids based on density-functional calculations, J. Phys. Chem. 97 (1993) 8617–8624. https://doi.org/10.1021/j100135a014.

[54] M.J. Mehl, D. Hicks, C. Toher, O. Levy, R.M. Hanson, G. Hart, S. Curtarolo, The AFLOW Library of Crystallographic Prototypes: Part 1, Computational Materials Science. 136 (2017) S1–S828. https://doi.org/10.1016/j.commatsci.2017.01.017.

[55] D. Hicks, M.J. Mehl, E. Gossett, C. Toher, O. Levy, R.M. Hanson, G. Hart, S. Curtarolo, The AFLOW Library of Crystallographic Prototypes: Part 2, Computational Materials Science. 161 (2019) S1–S1011. https://doi.org/10.1016/j.commatsci.2018.10.043.

[56] M. Ade, H. Hillebrecht, Ternary Borides Cr_2AlB_2, Cr_3AlB_4, and Cr_4AlB_6: The First Members of the Series $(CrB_2)_nCrAl$ with n = 1, 2, 3 and a Unifying Concept for Ternary Borides as MAB-Phases, Inorg. Chem. 54 (2015) 6122–6135. https://doi.org/10.1021/acs.inorgchem.5b00049.

[57] H. Zhang, F. Dai, H. Xiang, Z. Zhang, Y. Zhou, Crystal structure of Cr_4AlB_4: A new MAB phase compound discovered in Cr−Al−B system, Journal of Materials Science & Technology. 35 (2019) 530–534. https://doi.org/10.1016/j.jmst.2018.10.006.

[58] W. Rieger, H. Nowotny, F. Benesovsky, Die Kristallstruktur von Mo_2FeB_2, Monatshefte für Chemie. 95 (1964) 1502–1503. https://doi.org/10.1007/BF00901704.

[59] M. Mbarki, R.St. Touzani, B.P.T. Fokwa, Nb_2OsB_2, with a new twofold superstructure of the U_3Si_2 type: Synthesis, crystal chemistry and chemical bonding, Journal of Solid State Chemistry. 203 (2013) 304–309. https://doi.org/10.1016/j.jssc.2013.04.018.

[60] G. Hasemann, Experimental study of the liquidus surface in the V-rich portion of the V−Si−B system, Journal of Alloys and Compounds. 824 (2020) 153843. https://doi.org/10.1016/j.jallcom.2020.153843.

[61] R.S. Touzani, M. Krüger, First Principles Density Functional Theory Prediction of the Crystal Structure and the Elastic Properties of Mo_2ZrB_2 and Mo_2HfB_2, Crystals. 10 (2020) 865. https://doi.org/10.3390/cryst10100865.

[62] R.St. Touzani, C.W.G. Rehorn, B.P.T. Fokwa, Influence of chemical bonding and magnetism on elastic properties of the A_2MB_2 borides (A=Nb, Ta; M=Fe, Ru, Os) from first-principles calculations, Computational Materials Science. 104 (2015) 52–59. https://doi.org/10.1016/j.commatsci.2015.03.036.

[63] R.S. Touzani, J. Becker, M. Krüger, Site preference of V and its influence on the elastic properties in the boride series $V_xMo_{5-x}SiB_2$ as studied by first principles density functional theory, Journal of Alloys and Compounds. 819 (2020) 153041. https://doi.org/10.1016/j.jallcom.2019.153041.